Research Square

Preprints are preliminary reports that have not undergone peer review.
They should not be considered conclusive, used to inform clinical practice,
or referenced by the media as validated information.

Out-of-Plane Oscillating Electric Fields Unlock Low-Temperature Nonequilibrium Superionicity in Quasi-Two-Dimensional AgCrSe2

Jin Zhang

jinzhang@nanoctr.cn

National Center for Nanoscience and Technology, Chinese Academy of Sciences
https://orcid.org/0000-0001-7830-3464

Jia-Wen Li

National Center for Nanoscience and Technology, Chinese Academy of Sciences
https://orcid.org/0009-0003-7265-4687

Kun Yang

National Center for Nanoscience and Technology

Xinghua Shi

Chinese Academy of Sciences https://orcid.org/0000-0001-5012-3453

Sheng Meng

Institute of Physics, Chinese Academy of Sciences https://orcid.org/0000-0002-1553-1432

Weihai Fang

College of Chemistry, Key Laboratory of Theoretical & Computational Photochemistry of Ministry of Education, Beijing Normal University https://orcid.org/0000-0002-1668-465X

Article

Keywords:

Posted Date: November 3rd, 2026

DOI: https://doi.org/10.21203/rs.3.rs-11474705/v1

License: This work is licensed under a Creative Commons Attribution 4.0 International License.
Read Full License

Additional Declarations: There is **NO** Competing Interest.

Out-of-Plane Oscillating Electric Fields Unlock Low-Temperature Nonequilibrium Superionicity in Quasi-Two-Dimensional $AgCrSe_2$

Jia-Wen Li[1,2], Kun Yang[1,2], Sheng Meng[3,2,4], Xinghua Shi[1,2], Wei-Hai Fang[5], and Jin Zhang[1,2,*]

[1]Laboratory of Theoretical and Computational Nanoscience, National Center for Nanoscience and Technology, Chinese Academy of Sciences, Beijing 100190, China

[2]University of Chinese Academy of Sciences, Beijing 100049, China

[3]Beijing National Laboratory for Condensed Matter Physics, and Institute of Physics, Chinese Academy of Sciences, Beijing 100190, China

[4]Songshan Lake Materials Laboratory, Dongguan, Guangdong 523808, China

[5]College of Chemistry, Key Laboratory of Theoretical and Computational Photochemistry of Ministry of Education, Beijing Normal University, Beijing 100875, China

[*]jinzhang@nanoctr.cn

ABSTRACT

Superionic conductors enable exceptionally fast ion transport and offer broad technological potential, but their highly conductive states are typically accessible only above the mobile-ion sublattice order–disorder transition temperature. Here, electric-field-responsive machine-learning molecular dynamics reveals a nonequilibrium route to superionic transport in quasi-two-dimensional $AgCrSe_2$ under an out-of-plane oscillating electric field. At 300 K, far below the transition temperature near 475 K, the field activates fast in-plane Ag^+ transport with an ionic conductivity reaching ~1.7 S cm^{-1}. This originates from field-driven dynamic disorder of Ag^+ across two equivalent sublattices. The highly conductive, dynamically disordered state emerges when the driving half-period approaches the characteristic Ag-sublattice switching time, which shortens with increasing temperature and field amplitude. At strong fields, this timescale is consistent with field-assisted thermal activation, while weak-field deviations suggest additional dynamics. These results show timescale-matched periodic driving as a route to low-temperature nonequilibrium superionic transport.

Introduction

Superionic conductors (SICs) are characterized by exceptionally fast ion transport within a solid host, exhibiting ionic diffusivities and conductivities that can approach those of liquid electrolytes[1,2]. Upon crossing a characteristic order–disorder transition temperature T_{od}, the mobile-ion sublattice becomes dynamically disordered, enabling rapid liquid-like migration through the solid. Their exceptionally high ionic conductivity makes them promising candidates for various technological applications such as fuel cells and electrolysis cells[3,4], supercapacitors[5], intercalation MXenes[6], electrolytes in lithium-ion[7] and other solid-state batteries[8,9].

One outstanding limitation to the widespread application of many SICs is that their highly conductive superionic phases are stable only at elevated temperatures[10,11]. For example, the T_{od} of AgI and $AgCrSe_2$ are respectively 420 K and 475 K, substantially exceeding room temperature 300 K[12,13]. Many efforts have been devoted to overcoming this limitation to promote fast ionic transport at lower temperatures, including size control of α-AgI particles[14] and thickness reduction of $AgCrS_2$[15], compressive strain in Cu_2Se and Li_2Se[16], defect and vacancy engineering in LaH_x[4], Ag_2Te[17], LiB_3[18], and $AgCrSe_2$[19], as well as chemical substitution in KAg_3Se_2[20], Li_3YCl_6-type halides[21], Li_2ZrCl_6[22], and $CuCrSe_2$[23]. In contrast, electric fields can couple directly to ions, offering an effective route for manipulating ionic motion without modifying the material composition. Terahertz (THz) electric fields have been used to directly accelerate ionic hopping in β-aluminas[24,25], while selective excitation of TiO_6 rocking modes can substantially enhance Li^+ hopping in $Li_{0.5}La_{0.5}TiO_3$[26]. Conversely, ultrafast optical excitation can drive $AgCrSe_2$ into the superionic state by rapidly heating the system above its T_{od}, thereby activating fast Ag^+ migration[27]. However, whether oscillating electric fields can induce superionic transport below T_{od} remains largely unexplored.

In this work, we investigated the field-driven ionic dynamics of quasi-two-dimensional $AgCrSe_2$ using an electric-field-responsive machine-learning interatomic potential. An out-of-plane oscillating electric field is found to activate fast in-plane Ag^+ transport at 300 K, far below its equilibrium transition temperature T_{od} of 475 K, with a high ionic conductivity reaching 1.7 S cm^{-1}. This originates from field-driven Ag^+ redistribution between two equivalent sublattices, producing the dynamic occupation disorder characteristic of the high-temperature superionic phase and enabling fast ionic migration. Correspondingly, the ionic conductivity shows a pronounced positive correlation with the dynamic disorder of the Ag sublattices. As the frequency increases, the Ag occupation across the two sublattices evolves from complete switching, through a highly conductive dynamically disordered state, to a largely ordered state showing weak response. Increasing temperature or field amplitude shifts this dynamic picture toward higher frequencies. These behaviors reflect a competition between the driving period and the characteristic time for Ag ions to cross the migration barrier between two lattices. At strong fields, this timescale follows field-assisted thermal activation, whereas the additional slowdown at weak fields suggests dynamics beyond single-ion activation, such as the correlated Ag rearrangement. Together, these results reveal oscillating electric fields as a route to access low-temperature superionic transport, opening new possibilities for dynamically controlling superionic states.

Results

Order-disorder transition and ionic transport in $AgCrSe_2$

The crystal structure of $AgCrSe_2$ is shown in Figure 1(a), where Ag^+ ions are intercalated between the $CrSe_2$ layers. At low temperatures, Ag^+ ions predominantly occupy the α sites of the two symmetry-equivalent sublattices α and β (space group $R3m$). Above T_{od} = 475 K, the Ag sublattice becomes dynamically disordered with Ag^+ ions distributed equally over both sublattices ($R\bar{3}m$), and high ionic mobility[13,27–32].

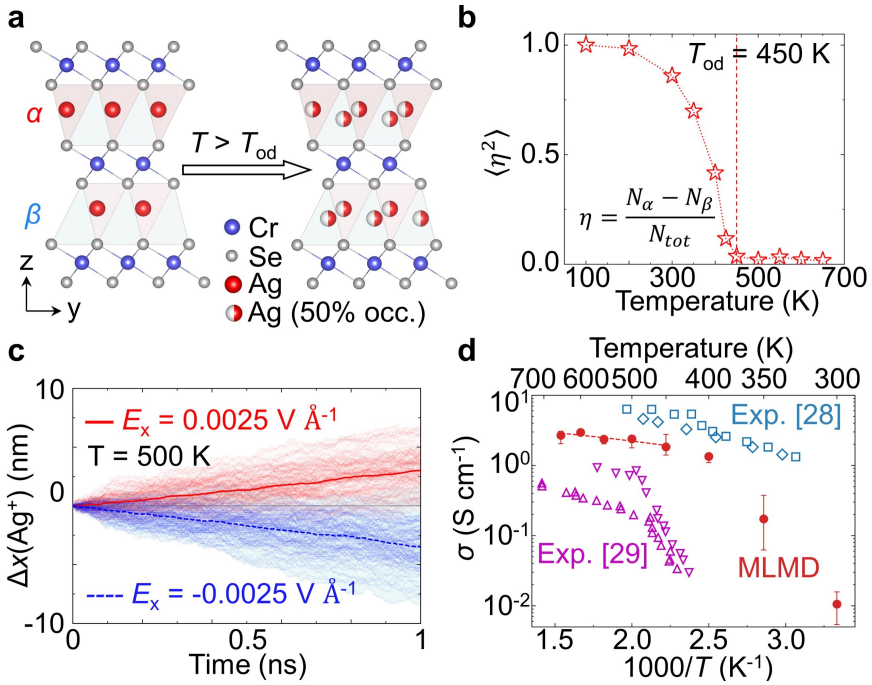


Figure 1. Order–disorder transition and ionic transport in $AgCrSe_2$. (**a**) Crystal structure of $AgCrSe_2$ and its order–disorder transition. At low temperature, Ag^+ ions predominantly occupy the α sublattice, whereas in the high-temperature superionic state they dynamically populate the symmetry-equivalent α and β sublattices with nearly equal probability. (**b**) Temperature dependence of $\langle\eta^2\rangle$, where $\eta = (N_\alpha - N_\beta)/N_{tot}$ and N_α (N_β) is the number of Ag ions occupying the α (β) sites. The collapse of $\langle\eta^2\rangle$ near 450 K marks $T_{od} \approx 450$ K, close to the experimental value of 475 K[27]. (**c**) Machine-learning molecular dynamics (MLMD) trajectories of Ag^+ at 500 K under $E_x = \pm 0.0025$ V $Å^{-1}$. Despite strong thermal fluctuations in individual trajectories, the ensemble-averaged displacement reverses with the applied field. (**d**) Temperature-dependent ionic conductivity from MLMD. Error bars span the simulated σ range at each temperature. Above 450 K, the conductivity follows Arrhenius behavior with an activation energy of 97 meV, whereas transport is strongly suppressed below 400 K. The calculated conductivities are consistent in magnitude and temperature dependence with experimental measurements[28,29].

To enable long-timescale simulations of Ag^+ dynamics, a machine-learning interatomic potential for $AgCrSe_2$ was trained using our electric-field-responsive graph neural network framework[33]. Machine-learning molecular dynamics (MLMD) extends first-principles-level simulations to substantially larger length and time scales and has been widely applied to materials simulations[33–40]. The dataset comprised 120 independent MD trajectories at 500–650 K in 50-K intervals, supplemented by low-temperature configurations at 300 and 400 K. The high-temperature superionic data were partitioned by trajectory to minimize correlations between subsets and prevent information leakage. The model shows high accuracy with mean absolute errors of 0.73 meV $atom^{-1}$ in energy and 33 meV

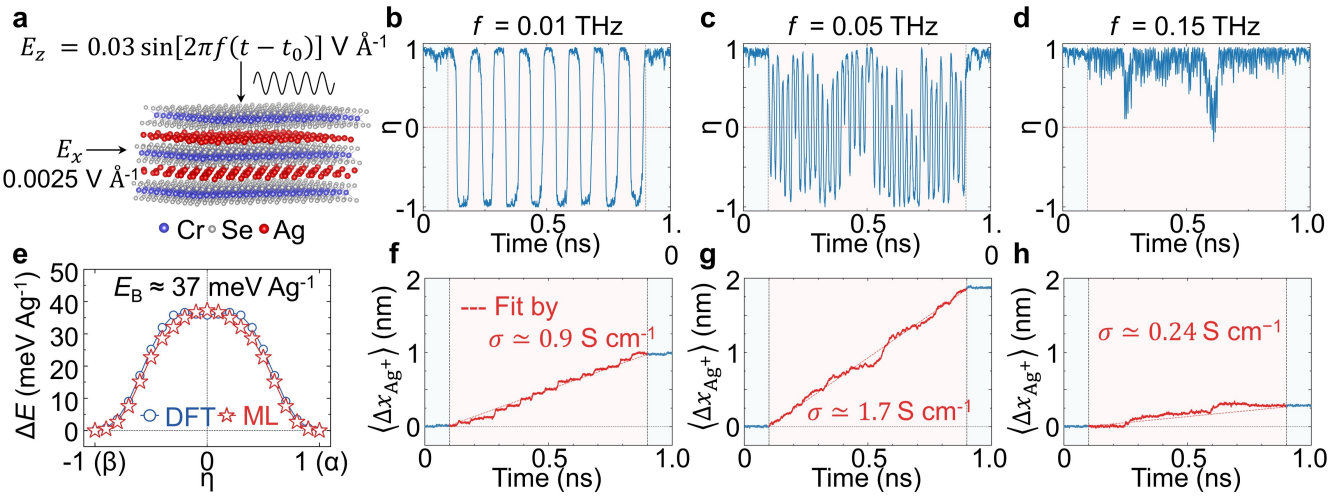


Figure 2. Frequency-dependent Ag-sublattice dynamics and ionic transport in $AgCrSe_2$ driven by out-of-plane oscillating fields at 300 K. (**a**) Schematic of the electric-field-driven MLMD. A sinusoidal out-of-plane field $E_z = 0.03\sin[2\pi f(t-t_0)]$ V Å^{-1} is applied, while an in-plane field E_x of 0.0025 V Å^{-1} probes Ag^+ transport. (**e**) The nudged elastic band energy profiles for the α–β transition from Density functional theory (DFT) and machine-learning (ML), showing consistent barriers of ~ 37 meV Ag^{-1}. (**b, f**) At frequency f = 0.01 THz, repeated switching of η between +1 and -1 reflects complete α–β switching of the Ag sublattice. Ag^+ displacement increases during the switching intervals but nearly plateaus in the ordered $|\eta| \simeq 1$ states, producing a stepwise displacement with $\sigma \simeq 0.9$ S cm^{-1}. (**c, g**) At f = 0.05 THz, rapid incomplete α–β oscillations are observed, producing a dynamically disordered state with conductivity of 1.7 S cm^{-1}. (**d, h**) At f = 0.15 THz, the Ag sublattice remains predominantly in the ordered state, with an ionic conductivity of 0.24 S cm^{-1}.

Å^{-1} in force, with further details provided in Supplementary Note 2.

To track the temperature dependence of Ag-sublattice order, MLMD simulations were performed in a 432-atom supercell, as shown in Fig. 1(b). Each Ag ion was assigned to the α or β sublattice according to the nearest reference site, with the order parameter defined as $\eta = (N_\alpha - N_\beta)/N_{tot}$, where N_α and N_β are the corresponding Ag populations and $N_{tot} = N_\alpha + N_\beta$. Thus, $\eta \simeq \pm 1$ denotes an ordered state dominated by one sublattice, whereas $\eta \simeq 0$ denotes comparable occupation of the two sublattices. As temperature increases, $\langle \eta^2 \rangle$ decreases sharply and approaches zero near 450 K, yielding $T_{od} \simeq 450$ K, close to the experimental value of 475 K[13,27–31].

The ionic conductivity was subsequently evaluated by MLMD under in-plane electric fields. The field was incorporated through the additional force $\mathbf{F}_i^{field} = \mathbf{Z}_i^* \mathbf{E}$, where $\mathbf{Z}_i^*$ is the configuration-dependent Born effective charge (BEC) tensor of atom i. The BECs were predicted with a neural network trained on the same configuration pool and partitioning protocol as the energy–force model, with metallic structures excluded based on the density of states at the Fermi level, yielding a mean absolute error of 0.10 e. The ionic conductivity was obtained as $\sigma_x = n_{Ag} e v_x / E_x$, where n_{Ag} is the Ag number density, e is the elementary charge, and v_x is the mean Ag drift velocity induced by the in-plane probe field E_x. At 500 K, the ensemble-averaged Ag^+ displacement reverses with $E_x = \pm 0.0025$ V Å^{-1} despite strong fluctuations in individual trajectories, as shown in Fig. 1(c). Conductivities were extracted from linear fits to the drift velocities at $E_x = \pm 0.0010$ and ± 0.0025 V Å^{-1} and are shown in Fig. 1(d). Above the calculated T_{od} ~ 450 K, the ionic conductivity remains high and follows Arrhenius behavior with a 97-meV activation energy consistent with previous reports[19,28,41], whereas it is strongly suppressed below 400 K. The calculated results provide reasonable estimates of the ionic conductivity and its temperature dependence compared with available experiments[28,29].

Temperature-dependent transport behavior and η in the MLMD trajectories are provided in Supplementary Notes 3 and 4.

Oscillating-field-induced disorder and ionic transport

We next examined the nonequilibrium Ag^+ dynamics under an out-of-plane oscillating electric field. As schematically illustrated in Fig. 2(a), a sinusoidal field $E_z(t) = E_z^0 \sin[2\pi f(t - t_0)]$ was applied, with E_z^0 and f denoting the field amplitude and frequency, while an in-plane field $E_x = 0.0025$ V Å^{-1} was used to probe Ag^+ transport. The associated α–β transition was further characterized by nudged elastic band calculations, as shown in Fig. 2(e), for which density functional theory and the machine-learning potential give consistent energy profiles and a barrier of approximately 37 meV per Ag. Under this driving protocol, MLMD simulations at 300 K and $E_z^0 = 0.03$ V Å^{-1} reveal three distinct frequency-dependent regimes: complete sublattice switching, a highly conductive dynamically disordered state, and, at higher frequencies, a largely ordered state with weak field response. Representative dynamics are shown in Fig. 2(b–d, f–h).

At a low frequency of $f = 0.01$ THz, the Ag sublattice undergoes repeated and complete α–β switching synchronized with the oscillating cycles, as shown in Fig. 2(b), reducing the time-averaged $\langle\eta^2\rangle$ from nearly 1 in the initial ordered state to ~ 0.76. Correspondingly, the ensemble-averaged Ag^+ displacement along E_x increases stepwise, with net drift occurring predominantly during the switching events and remaining negligible in the ordered $|\eta| \approx 1$ states. By contrast, Ag ions remain nearly immobile without the oscillating excitation. The resulting ionic conductivity reaches ~ 0.9 S cm^{-1}, nearly two orders of magnitude higher than the equilibrium value at 300 K in Fig. 1(d).

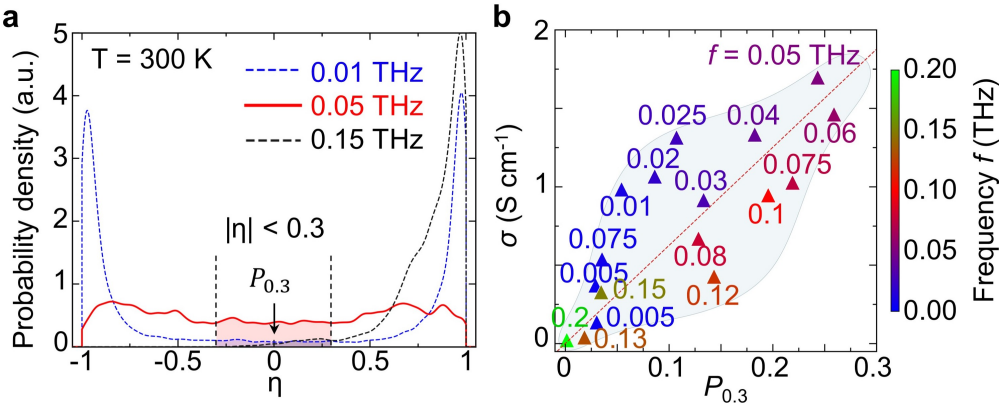


Figure 3. Correlation between field-induced dynamic disorder and ionic conductivity at 300 K. (**a**) Probability density of η at 300 K under different driving frequencies. $P_{0.3} = P(|\eta| < 0.3)$ quantifies the fraction of time spent in the dynamically disordered regime. (**b**) Distribution of σ and $P_{0.3}$ across different driving frequencies, revealing a clear positive correlation.

At $f = 0.05$ THz, the order parameter η exhibits rapid oscillations without fully completing the α–β transition, producing pronounced dynamic disorder with $\langle\eta^2\rangle \approx 0.38$ and an ionic conductivity of approximately 1.7 S cm^{-1}, close to that of the equilibrium superionic state, as evident in Fig. 2(c, g). As the frequency increases to 0.15 THz, the Ag sublattice remains predominantly in the initial α state and only rarely becomes the dynamically disordered $\eta \approx 0$ region, reducing the ionic conductivity to approximately 0.24 S cm^{-1}, as evident in Fig. 2(d, h). Notably,

the nanosecond-long simulations serve to ensure sufficient statistical sampling, rather than indicating a required nanosecond excitation duration.

To quantify the connection between dynamic disorder and ionic conductivity, the probability distribution of the order parameter η at different driving frequencies was analyzed. As shown in Fig. 3(a), the distribution is concentrated near $\eta \simeq \pm 1$ at f = 0.01 THz, becomes substantially broadened with significant weight around $\eta \simeq 0$ at f = 0.05 THz, and returns predominantly to the initial ordered state at f = 0.15 THz. Accordingly, a probability $P_{0.3} = P(|\eta| < 0.3)$ was introduced to quantify the residence in a highly disordered regime associated with superionic transport. Across the full frequency range from 0.005 THz to 0.200 THz, the ionic conductivity σ shows a pronounced positive correlation with $P_{0.3}$, as shown in Fig. 3(b). This trend is consistent with previous simulations[19]. The elemental temperatures remain centered near 300 K without sustained heating under the Langevin thermostat, as detailed in Supplementary Note 6, indicating that the enhanced transport is not thermally induced. This correlation indicates that enhanced Ag^+ transport is directly associated with oscillating-field-induced dynamic disorder of the Ag sublattice. Further transport analyses and $P_{0.3}$ statistics are provided in Supplementary Notes 6 and 7.

Field-driven dynamics and switching timescales

To systematically map the field-driven transport response, MLMD simulations were performed across different driving field amplitudes, frequencies, and temperatures. Based on the strong correlation between ionic conductivity and dynamic Ag-sublattice disorder, $P_{0.3}$ was adopted as an operational criterion, with $P_{0.3} \geq 10\%$ defining the transport-active regime and $P_{0.3} < 10\%$ the transport-suppressed regime. The field–frequency maps at 250 and 300 K reveal a clear high-frequency cutoff above which transport is suppressed. The cutoff shifts to higher frequencies with increasing field amplitude and temperature, demonstrating that stronger driving and thermal fluctuations allow the transport-active disordered state to persist under progressively faster oscillations. The evolution of this cutoff points to a characteristic switching timescale.

To extract this timescale, complete α–β switching was quantified through the switching probability P_{sw}, defined as the fraction of field periods in which η reaches both +0.6 and -0.6. The result at 300 K and E_z^0 = 0.03 V Å^{-1} with different frequencies is shown in Fig. 4(c). P_{sw} is nearly 1 at 0.01 THz, where the 50-ps half-cycle provides sufficient time for complete switching. As the frequency increases from approximately 0.02 to 0.1 THz, P_{sw} decreases sharply from nearly 1 to almost 0, demonstrating that complete switching becomes progressively suppressed as the available half-cycle duration is shortened. At 0.1 THz, the half-cycle is reduced to only 5 ps, which is insufficient for nearly all complete switching events. The characteristic switching frequency f_{sw} is taken as the frequency at which P_{sw} = 0.5, and the corresponding half-period, $\tau_{sw} = 1/(2f_{sw})$ is taken as the characteristic switching time. For T = 300 K and E_z^0 = 0.03 V Å^{-1}, f_{sw} is approximately 0.055 THz, corresponding to τ_{sw} ~ 9 ps.

The characteristic switching times τ_{sw} at 200, 250, and 300 K are shown as a function of E_z^0 in Fig. 4(d). A systematic acceleration of switching is observed upon either increasing the field amplitude or raising the temperature. In the strong-field regime, τ_{sw} exhibits a near-linear dependence on E_0 on the semilogarithmic plot, suggesting an exponential field dependence of the switching time. Accordingly, the strong-field data were described using a field-assisted thermal-activation model[42–44], $\tau_A = \tau_0 \exp\left[\frac{E_B - qE_z^0 d_z}{k_B T}\right]$. Here, τ_A is the characteristic time predicted by

the model, τ_0 is the attempt-time prefactor, E_B is the zero-field migration barrier, q is the charge of an Ag^+ ion, E_z^0 is the oscillating-field amplitude, d_z is the effective half-displacement of the Ag^+ ion projected along the field direction, k_B is the Boltzmann constant, and T is the temperature. With E_B = 37 meV, $q = +e$, and d_z = 0.33 Å, the strong-field data ($E_z^0 \geq 0.05$ V Å^{-1}) at all three temperatures are described using a single fitted prefactor τ_0 = 2.1 ps. As shown by the solid lines in Fig. 4(d), the resulting baseline provides a good description of the strong-field switching times at all three temperatures, consistent with thermally activated crossing of a field-lowered migration barrier. Details of P_{sw} and $P_{0.3}$ are provided in Supplementary Notes 7 and 8.

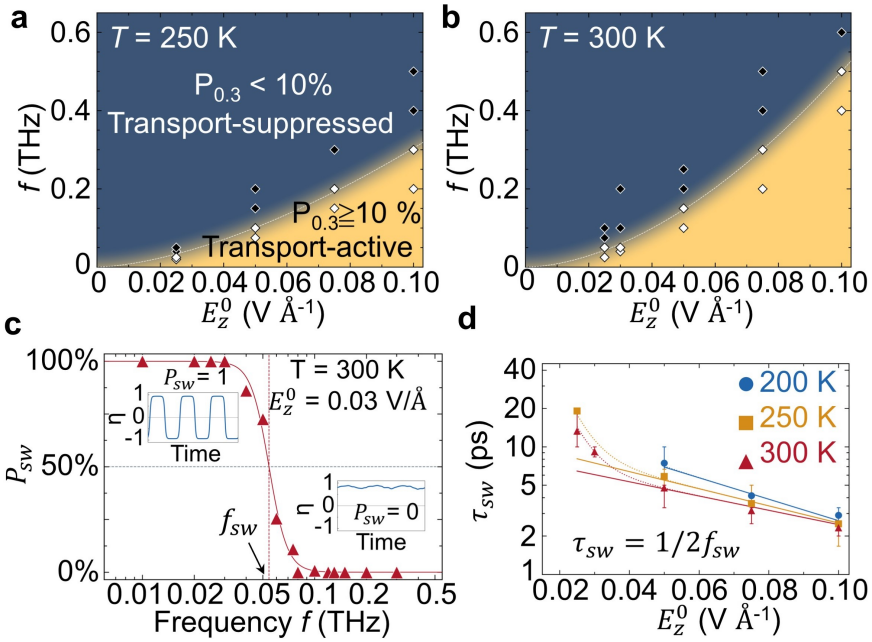


Figure 4. Field–frequency transport regimes and characteristic switching timescales. (a,b) Field–frequency diagrams at 250 and 300 K classified by $P_{0.3} = P(|\eta| < 0.3)$. The transport-active regime is defined by $P_{0.3} \geq 10\%$ (yellow), while $P_{0.3} < 10\%$ denotes transport suppression (blue), with open and filled diamonds marking the corresponding simulated conditions, respectively. **(c)** Switching probability P_{sw} at 300 K and E_z^0 = 0.03 V Å^{-1}. A complete switching event is counted when η reaches both +0.6 and −0.6 within one field cycle, and f_{sw} is defined by P_{sw} = 0.5. Insets schematically illustrate complete-switching and non-switching cases. **(d)** Characteristic switching time $\tau_{sw} = 1/(2f_{sw})$ at 200, 250, and 300 K. Error bars indicate the nearest sampled points on either side of P_{sw} = 0.5. Solid curves denote the strong-field Arrhenius baseline, while dotted curves include a phenomenological correction for the additional weak-field slowdown.

At weaker fields with $E_z^0 < 0.05$ V Å^{-1}, τ_{sw} rises markedly above the Arrhenius baseline, suggesting dynamics beyond simple local barrier crossing. This may reflect the additional time required for correlated ionic rearrangement preceding the α–β transition. Correlated Ag motion has been observed previously[19,27] and is also discovered in our MLMD trajectories (in Supplementary Note 5). In addition, the static calculations indicate eV-scale energetic penalties per transformed Ag for partial rearrangements involving either a single layer or a localized subset of Ag ions, far above the ~ 37 meV per Ag barrier for collective α–β motion. At weaker fields, such correlated configurations may require longer times to develop, thereby delaying access to the low-barrier pathway. Therefore we adopted a phenomenological weak-field enhancement of τ_A by $\tau_{sw} = \tau_A\left[1 + \exp(u - \beta E_z^0)\right]$. Here, u is a dimensionless parameter controlling the magnitude of the correction, while β determines its field dependence. The correction fac-

tor approaches unity at strong fields, recovering the field-assisted Arrhenius behavior, but increases rapidly as E_z^0 decreases, capturing the additional slowdown in the weak-field regime. With all Arrhenius parameters fixed at the values obtained from the strong-field analysis, only u and β were fitted globally to the data at all three temperatures, yielding $u = 4.5$ and $\beta = 173$. The resulting model describes the switching times over the full field range.

Discussion

In conclusion, using MLMD, we reveal that out-of-plane oscillating electric fields can activate nonequilibrium superionic transport in quasi-two-dimensional $AgCrSe_2$ far below its equilibrium order–disorder transition temperature. At 300 K, field-driven redistribution of Ag^+ between two equivalent sublattices produces a dynamically disordered state with an ionic conductivity reaching 1.7 $S\,cm^{-1}$. The resulting dynamics reflect a competition between the driving period and the characteristic response time of the Ag sublattice. With increasing frequency, the Ag sublattice evolves from complete switching to a highly conductive dynamically disordered regime, and finally to an ordered state with weak field response. The pronounced positive correlation between ionic conductivity and $P_{0.3} = P(|\eta| < 0.3)$ connects enhanced transport with sustained access to the dynamically disordered regime. Increasing either field amplitude or temperature shifts the transport-active regime toward higher frequencies, reflecting a faster Ag-sublattice response. In the strong-field regime, the switching timescale follows a field-assisted thermal-activation picture, whereas the additional weak-field slowdown suggests dynamics beyond simple barrier crossing, possibly involving correlated ionic rearrangement. No sustained heating is observed, indicating that the enhanced transport does not originate from a temperature-driven transition. Together, these results suggest oscillating electric fields as a promising approach for accessing low-temperature superionic transport through timescale matching, and dynamically tuning ionic transport properties.

Data availability

The data supporting the findings of this study are available from the corresponding author upon reasonable request.

Code availability

The custom code used in this study is available to editors and reviewers through a private repository during peer review and will be made publicly available upon publication.

References

1. Jun, K., Chen, Y., Wei, G., Yang, X. & Ceder, G. Diffusion mechanisms of fast lithium-ion conductors. *Nat. Rev. Mater.* **9**, 887–905, DOI: 10.1038/s41578-024-00715-9 (2024).
2. Sau, K. *et al.* Unlocking the secrets of ideal fast ion conductors for all-solid-state batteries. *Commun. Mater.* **5**, 122, DOI: 10.1038/s43246-024-00550-z (2024).
3. Liu, F. *et al.* Lowering the operating temperature of protonic ceramic electrochemical cells to < 450 ˚C. *Nat. Energy* **8**, 1145–1157, DOI: 10.1038/s41560-023-01350-4 (2023).

4. Zhang, W. *et al.* Deforming lanthanum trihydride for superionic conduction. *Nature* **616**, 73–76, DOI: 10.1038/s41586-023-05815-0 (2023).

5. Zhi, J., Zhao, S., Zhou, M., Wang, R. & Huang, F. A zinc-conducting chalcogenide electrolyte. *Sci. Adv.* **9**, eade2217, DOI: 10.1126/sciadv.ade2217 (2023).

6. Lukatskaya, M. R. *et al.* Cation intercalation and high volumetric capacitance of two-dimensional titanium carbide. *Science* **341**, 1502–1505, DOI: 10.1126/science.1241488 (2013).

7. Yin, Y.-C. *et al.* A $LaCl_3$-based lithium superionic conductor compatible with lithium metal. *Nature* **616**, 77–83, DOI: 10.1038/s41586-023-05899-8 (2023).

8. Kato, Y. *et al.* High-power all-solid-state batteries using sulfide superionic conductors. *Nat. Energy* **1**, 16030, DOI: 10.1038/nenergy.2016.30 (2016).

9. Boolchand, P. & Bresser, W. J. Mobile silver ions and glass formation in solid electrolytes. *Nature* **410**, 1070–1073, DOI: 10.1038/35074049 (2001).

10. Gu, W., Yang, X., Xiang, H., Zhang, L. & Feng, X. High temperature phase transitions in solid state electrolytes. *Curr. Opin. Electrochem.* **46**, 101537, DOI: 10.1016/j.coelec.2024.101537 (2024).

11. Feng, X. *et al.* Review of modification strategies in emerging inorganic solid-state electrolytes for lithium, sodium, and potassium batteries. *Joule* **6**, 543–587, DOI: 10.1016/j.joule.2022.01.015 (2022).

12. Hajibabaei, A., Baldwin, W. J., Csányi, G. & Cox, S. J. Symmetry breaking in the superionic phase of silver iodide. *Phys. Rev. Lett.* **134**, 026306, DOI: 10.1103/physrevlett.134.026306 (2025).

13. Ding, J. *et al.* Anharmonic lattice dynamics and superionic transition in $AgCrSe_2$. *Proc. Natl. Acad. Sci.* **117**, 3930–3937, DOI: 10.1073/pnas.1913916117 (2020).

14. Makiura, R. *et al.* Size-controlled stabilization of the superionic phase to room temperature in polymer-coated AgI nanoparticles. *Nat. Mater.* **8**, 476–480, DOI: 10.1038/nmat2449 (2009).

15. Peng, J. *et al.* Stoichiometric two-dimensional non-van der Waals $AgCrS_2$ with superionic behaviour at room temperature. *Nat. Chem.* **13**, 1235–1240, DOI: 10.1038/s41557-021-00800-4 (2021).

16. Dumett Torres, D. & Jain, P. K. Strain stabilization of superionicity in copper and lithium selenides. *J. Phys. Chem. Lett.* **9**, 1200–1205, DOI: 10.1021/acs.jpclett.8b00236 (2018).

17. Xu, Y., Xiang, X., Li, Z., Lu, Y. & Zhou, Y. Fast ionic transport governed by collective vibrational dynamics. *Phys. Rev. Lett.* **136**, 126302, DOI: 10.1103/hq41-8bt5 (2026).

18. Yang, S. *et al.* Defect enabled room temperature superionicity in 3D covalent mixed ionic electronic conductor lib_3. *J. Phys. Chem. Lett.* **17**, 7175–7181, DOI: 10.1021/acs.jpclett.6c01380 (2026).

19. Wang, J., Ding, J., Delaire, O. & Arya, G. Atomistic mechanisms underlying non-arrhenius ion transport in superionic conductor $AgCrSe_2$. *ACS Appl. Energy Mater.* **4**, 7157–7167, DOI: 10.1021/acsaem.1c01237 (2021).

20. Rettie, A. J. E. *et al.* A two-dimensional type I superionic conductor. *Nat. Mater.* **20**, 1683–1688, DOI: 10.1038/s41563-021-01053-9 (2021).

21. Liu, Z. *et al.* Tuning collective anion motion enables superionic conductivity in solid-state halide electrolytes. *Nat. Chem.* **16**, 1584–1591, DOI: 10.1038/s41557-024-01634-6 (2024).

22. Guan, C. *et al.* Triggering dynamically disordered lithium sublattice in superionic conductors. *Nat. Commun.* **17**, 4651, DOI: 10.1038/s41467-026-71304-3 (2026).

23. Rahman, M. T. *et al.* Controlling the order–disorder transition temperature through anion substitution in $CuCrX_2$ (X = S, Se, Te). *Chem. Mater.* **37**, 6718–6726, DOI: 10.1021/acs.chemmater.5c01384 (2025).

24. Minami, Y. *et al.* Macroscopic ionic flow in a superionic conductor Na^+ β-alumina driven by single-cycle terahertz pulses. *Phys. Rev. Lett.* **124**, 147401, DOI: 10.1103/physrevlett.124.147401 (2020).

25. Poletayev, A. D. *et al.* The persistence of memory in ionic conduction probed by nonlinear optics. *Nature* **625**, 691–696, DOI: 10.1038/s41586-023-06827-6 (2024).

26. Pham, K. H. *et al.* Correlated terahertz phonon–ion interactions control ion conduction in a solid electrolyte. *Mater. Horiz.* **13**, 3355–3375, DOI: 10.1039/d5mh01990g (2026).

27. Yang, J. *et al.* Tracking ultrafast ion diffusion dynamics in $AgCrSe_2$ superionic conductor. *Phys. Rev. X* **16**, 021024, DOI: 10.1103/s6rh-7219 (2026).

28. Murphy, D. W., Chen, H. S. & Tell, B. Superionic conduction in $AgCrS_2$ and $AgCrSe_2$. *J. Electrochem. Soc.* **124**, 1268–1271, DOI: 10.1149/1.2133543 (1977).

29. Boukamp, B. & Wiegers, G. Ionic and electronic processes in $AgCrSe_2$. *Solid State Ionics* **9-10**, 1193–1196, DOI: 10.1016/0167-2738(83)90151-0 (1983).

30. Li, B. *et al.* Liquid-like thermal conduction in intercalated layered crystalline solids. *Nat. Mater.* **17**, 226–230, DOI: 10.1038/s41563-017-0004-2 (2018).

31. Gascoin, F. & Maignan, A. Order–disorder transition in $AgCrSe_2$: a new route to efficient thermoelectrics. *Chem. Mater.* **23**, 2510–2513, DOI: 10.1021/cm200581k (2011).

32. Zhang, Z. *et al.* Discovery of robust interlocked ferroelectricity in 2D $AgCrSe_2$ via chemical vapor deposition. *Nanoscale* **18**, 2119–2130, DOI: 10.1039/d5nr04349b (2026).

33. Li, J.-W., Meng, S., Shi, X., Zhang, J. & Fang, W.-H. A unified graph neural network framework for non-equilibrium carrier and lattice dynamics driven by electric fields, DOI: 10.48550/ARXIV.2608.03287 (2026).

34. Batatia, I. *et al.* The design space of E(3)-equivariant atom-centred interatomic potentials. *Nat. Mach. Intell.* **7**, 56–67, DOI: 10.1038/s42256-024-00956-x (2025).

35. Wang, J. *et al.* E(n)-equivariant cartesian tensor message passing interatomic potential. *Nat. Commun.* **15**, 7607, DOI: 10.1038/s41467-024-51886-6 (2024).

36. Yu, H. *et al.* Prediction of room temperature ferroelectricity in subnano silicon thin films with an antiferroelectric ground state. *Phys. Rev. Lett.* **135**, 156801, DOI: 10.1103/xlkt-4wk5 (2025).

37. Thiemann, F. L. *et al.* Force-free molecular dynamics through autoregressive equivariant networks. *Nat. Mach. Intell.* **8**, 764–776, DOI: 10.1038/s42256-026-01227-7 (2026).

38. Libbi, F., Johansson, A., Kozinsky, B. & Monacelli, L. Nonequilibrium quantum dynamics in $SrTiO_3$ under impulsive THz radiation with machine learning. *Sci. Adv.* **11**, eadw1634, DOI: 10.1126/sciadv.adw1634 (2025).

39. Ke, C., Liu, F. & Liu, S. Superlubric motion of wavelike domain walls in sliding ferroelectrics. *Phys. Rev. Lett.* **135**, 046201, DOI: 10.1103/jhlq-2dd7 (2025).

40. Li, J.-W., Meng, S., Shi, X., Zhang, J. & Fang, W.-H. Domain-wall-mediated ultralow-barrier sliding and pinning in ferroelectric moiré superlattices revealed by machine learning, DOI: 10.48550/ARXIV.2604.20277 (2026).

41. Brüesch, P., Hibma, T. & Bührer, W. Dynamics of ions of the two-dimensional superionic conductor $AgCrS_2$. *Phys. Rev. B* **27**, 5052–5061, DOI: 10.1103/physrevb.27.5052 (1983).

42. Kemp, D. & De Souza, R. A. One stone, two birds: Using high electric fields to enhance the mobility and the concentration of point defects in ion-conducting solids. *J. Am. Chem. Soc.* **146**, 4783–4794, DOI: 10.1021/jacs.3c12843 (2024).

43. Menzel, S., Tappertzhofen, S., Waser, R. & Valov, I. Switching kinetics of electrochemical metallization memory cells. *Phys. Chem. Chem. Phys.* **15**, 6945, DOI: 10.1039/c3cp50738f (2013).

44. Salles, N. *et al.* Collective dipole effects in ionic transport under electric fields. *Nat. Commun.* **11**, 3330, DOI: 10.1038/s41467-020-17173-w (2020).

Acknowledgements

Jin Zhang acknowledges start-up support from the National Center for Nanoscience and Technology and funding from the National Natural Science Foundation of China (Grant No. 12574255). Jia-Wen Li acknowledges support from the Postdoctoral Fellowship Program (Grade C) of the China Postdoctoral Science Foundation (Grant No. GZC20261824). Xinghua Shi was supported by the National Key R&D Program of China (Grant No. 2022YFA1203200) and the National Natural Science Foundation of China (Grant No. 12125202). Sheng Meng acknowledges support from the Chinese Academy of Sciences (Grant No. YSBR-047) and the National Natural Science Foundation of China (Grant No. 12450401).

Author contributions

Jia-Wen Li and Jin Zhang conceived the original ideas and supervised the work. Jia-Wen Li performed the first-principles calculations, code development and data analysis. All authors participated in discussing and editing the manuscript.

Competing interests

The authors declare no competing interests.

Supplementary Files

This is a list of supplementary files associated with this preprint. Click to download.

- SM.pdf